

# Transition to time-periodicity of a natural-convection flow in a 3D differentially heated cavity

R. J. A. JANSSEN, R. A. W. M. HENKES and C. J. HOOGENDOORN

J. M. Burgers Centre, Department of Applied Physics, Delft University of Technology,  
P.O. Box 5046, 2600 GA Delft, The Netherlands

(Received 4 September 1992)

**Abstract**—The steady and time-periodic flow of air in a differentially heated cubical cavity has been studied numerically, using the finite-volume method. In the steady flow regime, the scaling in the boundary layer along the wall has been investigated. In the periodic flow regime, the calculated frequency was almost the same as for the two-dimensional square cavity, suggesting that the same instability mechanism is in both cases responsible for the bifurcation. There was, however, a strong three-dimensionality in the distribution of the amplitude of the oscillations.

## 1. INTRODUCTION

A LOT OF investigation in heat-transfer and fluid flow research in the past decades has been spent on studying natural-convection flows in rectangular cavities, both numerically and experimentally. Originally this effort was motivated by the many technical applications; later, this type of flow also became a popular test-case to compare numerical algorithms which are used to solve the Navier–Stokes equations.

The calculation of the steady laminar flow of air in a 2D square cavity with differentially heated sidewalls and adiabatic horizontal walls served as a comparison problem in a workshop organized by de Vahl Davis and Jones [1]. The flow was calculated for Rayleigh numbers up to  $10^6$ . Later, results for higher Rayleigh numbers have also been obtained. At higher Rayleigh numbers, the boundary layers in the cavity are thinner, making it more difficult to perform an accurate calculation.

More recently, interest in these flows has come from the study into the transition to turbulence that occurs when the Rayleigh number is increased to large values. The steady laminar flow loses its stability at a critical Rayleigh number of approximately  $1.75 \times 10^8$  and changes character through several so-called bifurcations until finally a fully turbulent state is established at a sufficiently large Rayleigh number. Accurate results for the first bifurcation of air in a two-dimensional square cavity with adiabatic horizontal walls have been obtained by Janssen and Henkes [2] using a finite-volume method to discretize the equations. However, they had to use grids with up to  $360 \times 360$  grid points to establish this accuracy. The critical Rayleigh number is considerably decreased if the adiabatic horizontal walls are replaced by perfectly conducting horizontal walls. Now, the first bifurcation occurs at Rayleigh numbers just beyond  $10^6$

and the boundary layers are still relatively thick, making it possible to use coarser grids and still obtain accurate results. Henkes [3] calculated the onset of the transition to turbulence with perfectly conducting horizontal walls in an air-filled cavity using grids with up to  $80 \times 80$  grid points and found that the first bifurcation was a Hopf-bifurcation originating from the corners of the cavity where the lower (upper) horizontal boundary layer hits the hot (cold) wall. The same problem was also addressed by several other authors: Le Quéré and Alziary de Roquefort [4, 5], Winters [6] and Jones and Briggs [7]. Especially Winters, who performed a linear stability of the *steady* flow, showed through grid refinement that his results were very accurate. The critical Rayleigh number calculated by Winters is  $2.1092 \times 10^6$ , which is in very good agreement with the value of  $2.10 \times 10^6$  obtained by Henkes [3].

All these calculations were performed using a *two*-dimensional geometry. Although Mallinson and de Vahl Davis [8] already performed calculations for the *three*-dimensional geometry, in which the horizontal and the lateral walls were taken adiabatic, they had to use very coarse grids (typically  $15^3$  grid points). Only now, after the development of more powerful computers and better numerical algorithms, is it becoming feasible to perform such calculations in a three-dimensional geometry for high Rayleigh numbers using appropriate grids. Le Peutrec and Lauriat [9] studied the heat losses through glazed side walls of air and water-filled enclosures for Rayleigh numbers up to  $10^7$ , using grids with up to  $41^3$  grid points. Fusegi *et al.* [10] calculated the steady heat transfer through an air-filled differentially heated cubical cavity with adiabatic horizontal walls for Rayleigh numbers up to  $10^6$  using grids with up to  $62^3$  grid points.

Especially for the investigation of the laminar-turbulent transition, three-dimensional calculations will

## NOMENCLATURE

|                   |  |               |  |
|-------------------|--|---------------|--|
| $A_r$             | ratio depth/height of cavity   | Greek symbols |  |
| $a$               | thermal diffusivity  | $\beta$       | coefficient of thermal expansion           |
| $f$               | frequency  | $\Gamma_\phi$ | diffusion coefficient for generic variable |
| $\mathbf{f}$      | flux vector  | $\delta$      | Kronecker-delta                            |
| $g$               | acceleration of gravity  | $\Delta$      | difference between two successive values   |
| $H$               | height of cavity   | $\nu$         | kinematic viscosity                        |
| $i_{\max}$        | number of grid points in $x$ -direction  | $\rho$        | density                                    |
| $\overline{Nu}$   | Nusselt number hot wall  | $\sigma$      | shear-stress                               |
| $\overline{Nu}_y$ | $y$ -averaged Nusselt number at hot wall   | $\phi$        | generic variable.                          |
| $Pr$              | Prandtl number, $\nu/\alpha$   |               |  |
| $p$               | pressure   | Superscript   |  |
| $Ra$              | Rayleigh number, $g\beta\Delta TH^3/\nu\alpha$                                       | $n$           | time-level.                                |
| $S$               | stratification in cavity centre  |               |  |
| $S_\phi$          | source term in generic equation  | Subscripts    |  |
| $T$               | temperature  | $i$           | $x$ -index grid point                      |
| $T_c$             | temperature of cold wall   | $j$           | $y$ -index grid point                      |
| $T_h$             | temperature of hot wall  | $k$           | $z$ -index grid point                      |
| $T_0$             | reference temperature  | E             | surface at $i+1/2$                         |
| $u_i$             | velocity component in the $x_i$ -direction   | W             | surface at $i-1/2$                         |
| $u_{\max}$        | maximum of $x$ -direction velocity along the vertical line through the cavity centre | N             | surface at $j+1/2$                         |
| $v_{\max}$        | maximum of vertical velocity along the horizontal line through the cavity centre     | S             | surface at $j-1/2$                         |
| $x_i$             | coordinate direction.  | F             | surface at $k+1/2$                         |
|                   |  | B             | surface at $k-1/2$ .                       |

be of interest. Since turbulence is a three-dimensional phenomenon, at some stage in the transition process instabilities in the third dimension must occur. The only three-dimensional calculation (to our knowledge) of the flow in the transitional regime in an air-filled cubical cavity with conducting horizontal walls, was carried out by Fusegi *et al.* [11]. They performed, however, only a calculation at a single Rayleigh number in the transition regime. They did not investigate any further the influence of the third dimension on the critical Rayleigh number of the flow and they did not discuss the character of the instability mechanism.

In the present investigation, 3D calculations were performed for air both in the steady and unsteady flow regimes. The horizontal walls were taken either adiabatic (in all instances resulting in steady flow) or perfectly conducting (resulting in either steady or periodic flow). The lateral walls were also taken to be either adiabatic or perfectly conducting. In the steady flow regime, some consideration is given to the boundary layer which, for Rayleigh numbers considered here ( $\geq 10^6$ ), develops along the walls perpendicular to the third dimension. Attention however, is focused primarily on calculating the flow near the critical Rayleigh number at which the first bifurcation occurs and on establishing the accuracy of the obtained results, by employing systematic grid refinement up to grids with  $120^3$  grid points. We compare these three-dimen-

sional results with results obtained by Henkes [3] for the two-dimensional cavity. It is investigated how the three-dimensionality of the flow influences both the kind of instability that occurs first and the critical Rayleigh number at which the instability appears. Also, it is studied how the structure of the oscillating flow is influenced by the presence of the lateral walls. Furthermore, it is investigated whether the two spatial symmetries, present in the steady flow below the critical Rayleigh number, are maintained after the bifurcation.

## 2. GOVERNING EQUATIONS

Considered is a cubical cavity with height, width and depth  $H$ , as depicted in Fig. 1. The left and right vertical walls are both isothermal; the left wall is hot with temperature  $T_h$ , and the right wall is cold with temperature  $T_c$ . The remaining four walls can be taken either adiabatic or conducting. The gravitation  $g$  acts in the negative  $x_2$ -direction. Air is the working fluid.

The flow in the cubical cavity is described by the three-dimensional, unsteady Navier-Stokes equations. Under the Boussinesq approximation, these equations read:

$$\frac{\partial u_i}{\partial x_i} = 0$$

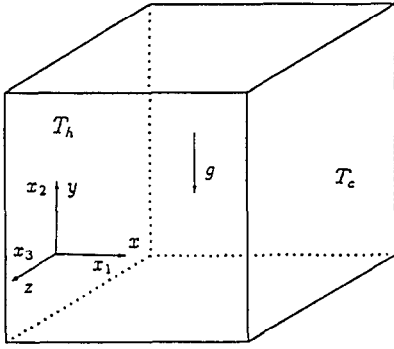


FIG. 1. The geometry under consideration. The height of the cavity is  $H$ .

$$\frac{\partial u_i}{\partial t} + \frac{\partial}{\partial x_j} (u_j u_i) = -\frac{1}{\rho} \frac{\partial p}{\partial x_i} + g\beta(T - T_0)\delta_{i2} + \nu \frac{\partial^2 u_i}{\partial x_j \partial x_j}$$

$$\frac{\partial T}{\partial t} + \frac{\partial}{\partial x_j} (u_j T) = a \frac{\partial^2 T}{\partial x_j \partial x_j}. \quad (1)$$

Here, the summation convention has been used, i.e. a summation (from 1 to 3) has to be performed over repeated indices in every term. In equations (1),  $u_i$  denotes the velocity component in the  $x_i$ -direction,  $t$  denotes time,  $\rho$  is the (constant) density,  $p$  is the pressure,  $\beta$  is the coefficient of thermal expansion,  $T$  is the temperature,  $T_0$  is a reference temperature,  $\delta$  is the Kronecker-delta,  $\nu$  is the kinematic viscosity and  $a$  the thermal diffusivity.

These equations can be made dimensionless using the length scale  $H$ , the time scale  $H/\sqrt{(g\beta\Delta TH)}$ , the temperature scale  $T_0 = (T_h + T_c)/2$  and the temperature difference  $\Delta T = T_h - T_c$ . This leads to a set of nondimensionalized equations which are governed by only two characteristic numbers: the Rayleigh number  $Ra \equiv g\beta\Delta TH^3/\nu a$  and the Prandtl number  $Pr \equiv \nu/a$ . In this study only air is considered with  $Pr = 0.71$ ; for air the only free parameter left is the Rayleigh number.

To fully specify the mathematical problem, both initial and boundary conditions have to be given. For the velocities we take the no-slip condition at all walls:

$$u_1 = u_2 = u_3 = 0 \quad \text{at} \quad x_1 = 0, H;$$

$$x_2 = 0, H; \quad x_3 = 0, H. \quad (2)$$

For the temperature, several boundary conditions will be considered. The left and right vertical walls are *always* isothermal:

$$T = T_h \quad \text{at} \quad x_1 = 0 \quad (3)$$

$$T = T_c \quad \text{at} \quad x_1 = H, \quad (4)$$

whereas the top/bottom horizontal ( $x_2 = 0, H$ ) and the back/front ( $x_3 = 0, H$ ) vertical walls can be taken as adiabatic:

$$\frac{\partial T}{\partial x_n} = 0 \quad \text{at} \quad x_n = 0, H \quad (n = 2, 3), \quad (5)$$

in which  $x_n$  denotes the coordinate normal to the wall. These walls can also be taken as perfectly conducting:

$$T = T_h - (x_1/H)(T_h - T_c) \quad \text{at} \quad x_n = 0, H \quad (n = 2, 3). \quad (6)$$

As initial condition we take either a solution obtained for a lower Rayleigh number or we take a previous solution for the same Rayleigh number but using a different number of grid points (if necessary, the solution is interpolated to the new grid). Our main interest is not in the transients but in the behaviour of the solution for large time.

For ease of notation, in the following  $x_1$ ,  $x_2$  and  $x_3$  will be denoted as  $x$ ,  $y$  and  $z$  respectively and  $u_1$ ,  $u_2$  and  $u_3$  will be denoted as  $u$ ,  $v$  and  $w$  respectively.

### 3. DISCRETIZATION AND SOLVER

#### 3.1. Finite-volume method

The equations (1) are discretized by the finite-volume method, as introduced by Patankar and Spalding [12]. The finite-volume method divides the computational domain into rectangular volumes. Unknown  $u$ -velocities are positioned in the middle of the left and right vertical sides of the finite volume,  $v$ -velocities are positioned in the middle of the horizontal sides and  $w$ -velocities are positioned in the middle of the front and back vertical sides. Scalar unknowns ( $p$  and  $T$ ) are positioned in the centre of the finite volume. This staggered-grid concept was introduced by Harlow and Welch [13] and has advantages in discretizing the pressure gradients in combination with the continuity equation.

To explain the finite-volume method we consider the three-dimensional convection-diffusion equation for the generic variable  $\phi$ :

$$\frac{\partial \phi}{\partial t} + \nabla \cdot \mathbf{f} = S_\phi. \quad (7)$$

Here,  $\mathbf{f}$  is the flux vector and  $S_\phi$  is a source term. The flux vector is the sum of a convection part  $\mathbf{f}^c = \mathbf{u}\phi$  and a diffusion part  $\mathbf{f}^d = -\Gamma_\phi \nabla \phi$ . Equation (7) is integrated over the finite volume around grid point  $(i, j, k)$ , rewriting  $\nabla \cdot \mathbf{f}$  as fluxes through the sides of the  $(i, j, k)$ -volume with the help of Gauss' divergence theorem. (The integration is performed over the finite volumes around the staggered grid points for the velocities  $u$ ,  $v$  and  $w$  if the momentum equations are considered). We obtain:

$$\int_{\text{vol. } i,j,k} \frac{\partial \phi}{\partial t} dx dy dz + \int_{\text{side}} [f_E - f_W] dy dz$$

$$+ \int_{\text{side}} [f_N - f_S] dx dz + \int_{\text{side}} [f_F - f_B] dx dy$$

$$= \int_{\text{vol. } i,j,k} S_\phi dx dy dz. \quad (8)$$

The subscripts E, W, N, S, F and B refer to the east,

west, north, south, front and back side of the volume respectively. The remaining integrals are approximated as :

$$\begin{aligned} & \left(\frac{\partial \phi}{\partial t}\right)_{i,j,k} \Delta x \Delta y \Delta z + [f_{i+1/2,j,k} - f_{i-1/2,j,k}] \Delta y \Delta z \\ & + [f_{i,j+1/2,k} - f_{i,j-1/2,k}] \Delta x \Delta z + [f_{i,j,k+1/2} - f_{i,j,k-1/2}] \Delta x \Delta y \\ & = (S_\phi)_{i,j,k} \Delta x \Delta y \Delta z + \Delta x \Delta y \Delta z O(\Delta x^2, \Delta y^2, \Delta z^2), \quad (9) \end{aligned}$$

in which the size of the grid is  $\Delta x = x_{i+1/2} - x_{i-1/2}$ ,  $\Delta y = y_{j+1/2} - y_{j-1/2}$  and  $\Delta z = z_{k+1/2} - z_{k-1/2}$ . The finite-volume method has the advantage that it gives a conservative discretization: numerical mass, momentum and heat fluxes can be indicated that are conserved over the domain. The integration in time in equation (9) is performed fully implicitly: all spatial derivatives are evaluated at the new time level  $n$ . The unsteady term, the fluxes and the source are further discretized with finite differences. The unsteady term at the time level  $n$  is discretized with three time levels, giving a second-order truncation error in time:

$$\left(\frac{\partial \phi}{\partial t}\right)_{i,j,k}^{(n)} = \frac{3\phi_{i,j,k}^{(n)} - 4\phi_{i,j,k}^{(n-1)} + \phi_{i,j,k}^{(n-2)}}{2\Delta t} + O(\Delta t^2). \quad (10)$$

Here  $\Delta t$  denotes the constant time step size  $t^{(n)} - t^{(n-1)}$ . The diffusion part of the flux is discretized with a second-order truncation error:

$$f_{i+1/2,j,k}^d = -\Gamma_\phi \frac{\phi_{i+1,j,k} - \phi_{i,j,k}}{x_{j+1} - x_j} + O(\Delta x^2). \quad (11)$$

In order to discretize the convection flux, it is rewritten as:

$$f_{i+1/2,j,k} = u_{i+1/2,j,k} \phi_E, \quad (12)$$

where  $\phi_E$  is an approximation for  $\phi$  at the east side of the volume ( $i, j, k$ ). In the discretization of the temperature equation the convecting velocity  $u$  has a grid point precisely at the east side of the volume, and no further interpolation for  $u$  is needed. For the  $u, v$  and  $w$  equations the value for the velocity at the side is found from taking the average value of two neighbouring grid points. For the convection, the following discretization was used:

$$\phi_E = \frac{1}{2}(\phi_{i,j,k} + \phi_{i+1,j,k}), \quad (13)$$

which leads to the well-known central-differencing scheme for the convection.

The pressure plays a peculiar role in the incompressible Navier-Stokes equations, because the pressure does not appear in the continuity equation. Therefore, the continuity equation acts as a *constraint* on the velocity field: the pressure has to be determined such that the velocity field in the momentum equation satisfies the continuity equation. This implies that the divergence operator in the continuity equation and the gradient operator for the pressure in the momentum equation are closely related. Careless discretization of

the continuity equation and the pressure gradient can lead to a large numerical inaccuracy (wiggles) in the pressure. For a two-dimensional geometry, Van Kan [14] shows that the finite-volume method on a staggered grid leads to a proper discretization. If his results are extended to the three-dimensional geometry, this gives:

$$\begin{aligned} & \frac{u_{i+1/2,j,k} - u_{i-1/2,j,k}}{\Delta x} + \frac{v_{i,j+1/2,k} - v_{i,j-1/2,k}}{\Delta y} \\ & + \frac{w_{i,j,k+1/2} - w_{i,j,k-1/2}}{\Delta z} = O(\Delta x^2, \Delta y^2, \Delta z^2) \quad (14a) \end{aligned}$$

$$\left(\frac{\partial p}{\partial x}\right)_{i+1/2,j,k} = \frac{p_{i+1,j,k} - p_{i,j,k}}{\Delta x} + O(\Delta x^2) \quad (14b)$$

$$\left(\frac{\partial p}{\partial y}\right)_{i,j+1/2,k} = \frac{p_{i,j+1,k} - p_{i,j,k}}{\Delta y} + O(\Delta y^2) \quad (14c)$$

$$\left(\frac{\partial p}{\partial z}\right)_{i,j,k+1/2} = \frac{p_{i,j,k+1} - p_{i,j,k}}{\Delta z} + O(\Delta z^2). \quad (14d)$$

Here the discretization of the continuity equation is found by integration over the finite volume ( $i, j, k$ ). The discretizations of the  $x, y$  and  $z$  pressure gradient appear as the sources  $S_x, S_y$  and  $S_z$  in the momentum equations.

### 3.2. Grid distribution

The grid is constructed by firstly distributing the velocity grid lines according to a stretching function. This distribution is such that the boundaries of the physical domain coincide with velocity grid lines. Secondly, the scalar points are placed precisely in the centre of the scalar volumes. For the  $u$ -velocities the stretching function is chosen as:

$$\frac{x_i}{H} = \frac{i}{i_{\max}} - \frac{1}{2\pi} \sin\left(2\pi \frac{i}{i_{\max}}\right) \quad i = 0, 1, \dots, i_{\max}. \quad (15)$$

The same distribution function is used to distribute the  $v$ - and  $w$ -velocities. This distribution concentrates grid points in the boundary layers along the walls.

In order to discretize the boundary conditions, the grid is extended across the boundaries, introducing one extra (virtual) grid point. Dirichlet boundary conditions for the temperature are discretized with second-order accuracy, using the virtual point. For example:

$$T_{\text{boundary}} = \frac{T_{i_{\max}+1,j,k} + T_{i_{\max},j,k}}{2} + O(\Delta x^2), \quad (16)$$

where  $i_{\max} + 1$  denotes the virtual point. Homogeneous Neumann boundary conditions for the temperature are applied by setting the value at the virtual point equal to the value at the first inner grid point, which also gives a second-order accurate discretization. The no-slip boundary conditions for  $u$  at the west and east boundaries, for  $v$  at the north and south

boundaries and for  $w$  at the front and back boundaries are applied by setting all velocity grid points at the boundaries to zero. The zero boundary conditions for the velocities at the boundaries in the non-staggered coordinate directions are applied by using a virtual point, leading to an equation similar to equation (16).

### 3.3. Solution method

As an implicit method is used to discretize the time-dependent equations, at each new time level  $n$  a system of nonlinear algebraic equations has to be solved. The solving of the different transport equations (for  $u$ ,  $v$ ,  $w$  and  $T$ ) is decoupled. The discrete systems belonging to each of the transport equations are iteratively solved by a line Gauss–Seidel method. Alternating Gauss–Seidel sweeps are made from the back to the front and from the front to the back side of the computational domain. During a sweep from the back to the front sides, at each plane of constant  $z$ , a sweep is performed from the west to the east side of the computational domain. During a sweep from the front to the back side, at each plane of constant  $z$ , a sweep is performed from the east to the west side of the domain. To update the solution at line  $i$  in a sweep from the back to the front side, contributions of line  $i-1$  at the current  $z$ -plane and line  $i$  at the previous  $z$ -plane are evaluated at the new iteration (sweep) level, whereas contributions of the line  $i+1$  at the current  $z$ -plane and line  $i$  at the next  $z$ -plane are evaluated at the previous iteration (sweep) level. In a sweep from the front to the back side, the reverse holds. All nonlinearities at the line  $i$  are evaluated at the previous iteration level, whereas all other contributions of line  $i$  are treated implicitly. As a result, during the sweep only a tridiagonal matrix for each variable remains to be solved at line  $i$ . This tridiagonal matrix is solved directly. Line coupling is used to iteratively couple the different transport equations: in each Gauss–Seidel sweep the different variables ( $u$ ,  $v$ ,  $w$  and  $T$ ) are updated one after the other at a line.

After each sweep the pressure is calculated from a pressure-correction equation. During sweep  $l$  the pressure is evaluated at the previous iteration level  $l-1$ . After this sweep the iterative velocity field  $u^*$ ,  $v^*$ ,  $w^*$  is obtained. The prediction of this velocity field is corrected according to:

$$u_{i+1/2,j,k} = u_{i+1/2,j,k}^* + \frac{du}{dp} (p'_{i,j,k} - p'_{i+1,j,k}) \quad (17a)$$

$$v_{i,j+1/2,k} = v_{i,j+1/2,k}^* + \frac{dv}{dp} (p'_{i,j,k} - p'_{i,j+1,k}) \quad (17b)$$

$$w_{i,j,k+1/2} = w_{i,j,k+1/2}^* + \frac{dw}{dp} (p'_{i,j,k} - p'_{i,j,k+1}) \quad (17c)$$

in which  $p'$  is the pressure correction. These expressions are found by linearizing the velocities at the new time level in the unsteady term of the momentum equations with respect to the pressure gradient

(i.e.  $du/dp = 2\Delta t/3\rho\Delta x$ ,  $dv/dp = 2\Delta t/3\rho\Delta y$  and  $dw/dp = 2\Delta t/3\rho\Delta z$ ). Substitution of equations (17) in the discretized continuity equation (14a) gives the equation for the pressure correction, which is nothing but a discretization of a Poisson equation for  $p'$ :

$$\frac{\partial^2 p'}{\partial x^2} + \frac{\partial^2 p'}{\partial y^2} + \frac{\partial^2 p'}{\partial z^2} = \frac{3}{2} \frac{\rho}{\Delta t} \left( \frac{\partial u^*}{\partial x} + \frac{\partial v^*}{\partial y} + \frac{\partial w^*}{\partial z} \right). \quad (18)$$

At the walls a zero gradient correction is prescribed. When the Gauss–Seidel process is fully converged the right-hand side of equation (18) vanishes, giving a zero pressure correction. Discretization of equation (18) gives a symmetric band-matrix for the pressure correction, which has only seven diagonals with non-zero entries. Probably the best way to solve the resulting set of equations when a nonuniform grid is employed, is to use an iterative solver. Our solver was based on the preconditioned conjugate gradient method, as described by Meijerink and Van der Vorst [15] and by Van der Vorst [16]. In this method, a (Modified) Incomplete Cholesky decomposition of the band-matrix is used to transform the original system of equations into an equivalent system that is much better suited (better conditioned) to be solved by the Conjugate Gradient method. The resulting solver will be denoted as the (M)ICCG-solver. It is known that this (M)ICCG-solver has a much higher rate of convergence than the original CG-method. We checked that the convergence rate of the (M)ICCG-solver was indeed very high: as a rule five iterations were performed in every sweep. However, straightforward implementation of the preconditioned algorithm on vectorcomputers turns out to give a disappointing performance because the preconditioning part of the algorithm is not completely vectorizable. This is because triangular systems have to be solved, giving first order recurrences. Several authors have considered this problem in the past (e.g. Dubois *et al.* [17] and Van der Vorst [18]) and suggested solutions to this problem that were, at least partially, successful. In our implementation, the unknowns are reordered explicitly along the so-called hyperplanes in the computational domain (hyperplanes are planes for which the sum  $i+j+k$  of the grid point indices  $i$ ,  $j$  and  $k$  is constant). Use of this approach results in a code that is vectorizable, in turn for an increase in the number of operations that have to be performed during one iteration of the (M)ICCG-algorithm as compared to the straightforward implementation of the algorithm. A more detailed description of this approach, is given by Schlichting and Van der Vorst [19].

The sweep process at each time level was stopped when the dimensionless pressure-correction in each grid point and the dimensionless net heat flux through the boundaries were below the criterion of  $10^{-4}$ . Typically 10–15 sweeps were necessary to reach this criterion.

#### 4. STEADY FLOW RESULTS

As a test-case, calculations were performed for  $Ra = 10^6$  in which the top/bottom ( $y = 0, H$ ) and front/back walls ( $z = 0, H$ ) of the cubical cavity were taken adiabatic. This is the configuration for which most of the three-dimensional calculations for air, existing in literature, have been performed.

The governing system of equations (1) allows two spatial symmetries in the solution. Firstly, the solution can be symmetric around the line  $(H/2, H/2, z)$ :

$$\begin{aligned} u(x, y, z, t) &= -u(H-x, H-y, z, t) \\ v(x, y, z, t) &= -v(H-x, H-y, z, t) \\ w(x, y, z, t) &= w(H-x, H-y, z, t) \\ T(x, y, z, t) &= (T_h + T_c) - T(H-x, H-y, z, t) \\ p(x, y, z, t) &= p(H-x, H-y, z, t). \end{aligned} \quad (19)$$

Secondly, it can be symmetric in the plane  $z = H/2$ ,

$$\begin{aligned} u(x, y, z, t) &= u(x, y, H-z, t) \\ v(x, y, z, t) &= v(x, y, H-z, t) \\ w(x, y, z, t) &= -w(x, y, H-z, t) \\ T(x, y, z, t) &= T(x, y, H-z, t) \\ p(x, y, z, t) &= p(x, y, H-z, t). \end{aligned} \quad (20)$$

The present boundary conditions admit the same two symmetries. To reduce the computational effort required to solve the set of equations (1), these two symmetries were exploited to perform calculations over only a quarter of the entire enclosure.

Grids with  $16^3$ ,  $30^3$ ,  $60^3$  and  $120^3$  grid points were used (these numbers are the number of grid points over the entire domain, i.e. in the case of a symmetric computation the actual number of grid points employed in the calculation is a quarter of the above-mentioned numbers). To check the correctness of the assumption of spatial symmetry, a calculation was performed employing a  $30^3$  grid without using the symmetry. The results checked to be the same as those obtained in the symmetric calculation on the same grid. Therefore, all subsequent calculations for this Rayleigh number were performed exploiting the spatial symmetries.

The results of these calculations, together with

those of previous studies are given in Table 1. Haldenwang and Labrosse [20] used a pseudo-spectral method with  $33 \times 33 \times 29$  spectral functions to obtain their results; Le Peutrec and Lauriat [9] employed a finite-difference method with  $41^3$  grid points; Fusegi *et al.* [10] used a finite-volume method with  $62^3$  grid volumes. Also tabulated in Table 1 are results obtained for the two-dimensional square cavity with adiabatic horizontal walls. These 2D results were obtained using grids with up to  $240^2$  grid points and were checked to be grid independent. The same values for the two-dimensional cavity, up to four decimals, were obtained by Le Quéré [21] who used a pseudo-spectral method with up to  $128 \times 128$  spectral functions.

Four quantities are tabulated in Table 1:  $\overline{Nu}$ , which is the dimensionless heat flux through the hot vertical wall:

$$\overline{Nu} = -\frac{1}{H\Delta T} \int_{z=0}^z \int_{y=0}^{y=H} \left( \frac{\partial T}{\partial x} \right)_{x=0} dy dz; \quad (21)$$

$v_{\max}$ , the maximum of the vertical velocity along the line  $(x, H/2, H/2)$  (i.e. the horizontal line in the vertical midplane  $z = H/2$  through the centre of the cavity);

$u_{\max}$ , the maximum of the horizontal velocity along the vertical line  $(H/2, y, H/2)$  and the stratification  $S$  ( $\equiv (H/\Delta T)(\partial T/\partial y)$ ) in the cavity centre  $(H/2, H/2, H/2)$ . The velocity maxima  $u_{\max}$  and  $v_{\max}$  have been determined from a Lagrangian interpolation, using a second-order polynomial. The quantities tabulated in Table 1 have been scaled;  $\overline{Nu}$  with  $Ra^{-1/4}$ ,  $v_{\max}$  with  $(g\beta\Delta TH)^{1/2}$  and  $u_{\max}$  with  $(g\beta\Delta T\nu)^{1/3}$ . In a detailed analysis of the scalings in the two-dimensional square cavity, Henkes [3] has shown that these are indeed the proper scalings.

As can be seen in Table 1, our results show that a high accuracy has been obtained. Roughly speaking, the calculated results are in the asymptotic regime for  $\overline{Nu}$ ,  $u_{\max}$  and  $S$ , i.e. the differences between the values on successive grids decrease approximately quadratically with the number of grid points. For  $v_{\max}$  this is almost the case. Our results are in good agreement with those of Fusegi *et al.* [10] except for  $u_{\max}$  for which there is a difference of 3.9% with the value we have obtained on our finest grid. Also, the differences between the values obtained for the two-dimensional

Table 1. Grid dependence of characteristic quantities for air at  $Ra = 10^6$  with the horizontal and lateral walls adiabatic

| Grid                          | $\overline{Nu} Ra^{-1/4}$ | $v_{\max}/(g\beta\Delta TH)^{1/2}$ | $u_{\max}/(g\beta\Delta T\nu)^{1/3}$ | $S$    |
|-------------------------------|---------------------------|------------------------------------|--------------------------------------|--------|
| $16^3$                        | 0.2705                    | 0.2962                             | 0.8509                               | 0.9719 |
| $30^3$                        | 0.2725                    | 0.2620                             | 0.8634                               | 0.9293 |
| $60^3$                        | 0.2730                    | 0.2597                             | 0.8585                               | 0.9138 |
| $120^3$                       | 0.2732                    | 0.2585                             | 0.8575                               | 0.9103 |
| Haldenwang <i>et al.</i> [20] | 0.2723                    | ---                                | ---                                  | ---    |
| Le Peutrec <i>et al.</i> [9]  | 0.2738                    | ---                                | ---                                  | ---    |
| Fusegi <i>et al.</i> [11]     | 0.2773                    | 0.2588                             | 0.8910                               | ---    |
| 2D ( $240^2$ )                | 0.2791                    | 0.2618                             | 0.8146                               | 0.9132 |

geometry and those for the three-dimensional geometry are small; the largest difference (5.0%) occurs for  $u_{\max}$ . These results suggest that for the cubical cavity at  $Ra = 10^6$ , the flow in the vertical midplane ( $z = H/2$ ) can in good approximation be considered as two-dimensional.

The effects of the lateral walls of the cavity, perpendicular to the  $z$ -direction, can be seen clearly in the  $z$ -dependence of  $\overline{Nu}_z$ , which has been plotted in Fig. 2(a) for  $Ra = 10^6$ . Here,  $\overline{Nu}_z$  is the  $y$ -averaged Nusselt number at the hot wall:

$$\overline{Nu}_z = -\frac{1}{\Delta T} \int_{y=0}^{y=H} \left( \frac{\partial T}{\partial x} \right)_{x=0} dy. \quad (22)$$

The  $y$ -averaged Nusselt number decreases strongly as the lateral walls are approached. A similar behaviour can be found in  $z$ -profiles of the vertical velocity; in Fig. 2(b) the  $z$ -dependence of  $v_{\max}$  has been depicted (i.e. in every plane  $z = \text{constant}$ ,  $v_{\max}$  at  $y = H/2$  has been calculated just as for the mid-plane  $z = H/2$  and the velocity profile has been plotted). Noteworthy is that  $v_{\max}(z)$  has a local maximum close to the lateral walls (in Fig. 2(b) located at  $z = 0.068H$ ). A behaviour of this kind was predicted analytically by Bödewadt [22] for the cylindrical forced-convection flow of an incompressible fluid over a flat plate, in which the fluid at infinite distance from the plate was moving with constant angular velocity. Bödewadt employed assumptions used in boundary-layer theory to perform his analysis. For values of the Rayleigh number considered here ( $\sim 10^6$ ), boundary layers will develop along the lateral walls. In the literature, relatively

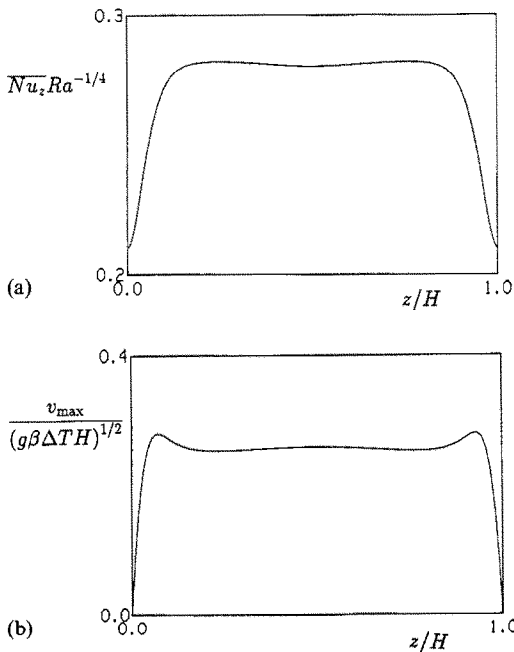


FIG. 2. Three-dimensionality of the steady flow of air in the cubical cavity at  $Ra = 10^6$  with adiabatic horizontal walls. (a)  $\overline{Nu}_z$  as a function of depth ( $z$ ); (b)  $v_{\max}$  as a function of depth.

little attention has been paid to these boundary layers. Contrary to this, the boundary layer along the hot wall in the two-dimensional cavity has been the subject of much investigation (especially concerning the scaling of the boundary layer, see e.g. Gill [23], Graebel [24] and Henkes [3]). To investigate the nature of the flow near the wall  $z = 0$ , the shear stresses  $\sigma_{13}$  and  $\sigma_{23}$  have been calculated in the plane  $z = 0$ . Here,  $\sigma_{13}$  and  $\sigma_{23}$  are given by:

$$\sigma_{13} = \rho\nu \left( \frac{\partial u}{\partial z} + \frac{\partial w}{\partial x} \right) \quad (23a)$$

$$\sigma_{23} = \rho\nu \left( \frac{\partial v}{\partial z} + \frac{\partial w}{\partial y} \right). \quad (23b)$$

The results of these calculations (for  $Ra = 10^6$ ) are given in Figs. 3(a) and (b), in which respectively the shear-stress vectors and the shear-stress magnitudes ( $\sqrt{\sigma_{13}^2 + \sigma_{23}^2}$ ) are given. Clearly, the shear stresses have the largest magnitude in regions near the hot and cold walls. For comparison purposes, the *stream lines* in the 2D square cavity for  $Ra = 10^6$  have been plotted in Fig. 4. If Figs. 3(a) and 4 are compared, it is clear that the shear stresses in the plane  $z = 0$  of the cubical

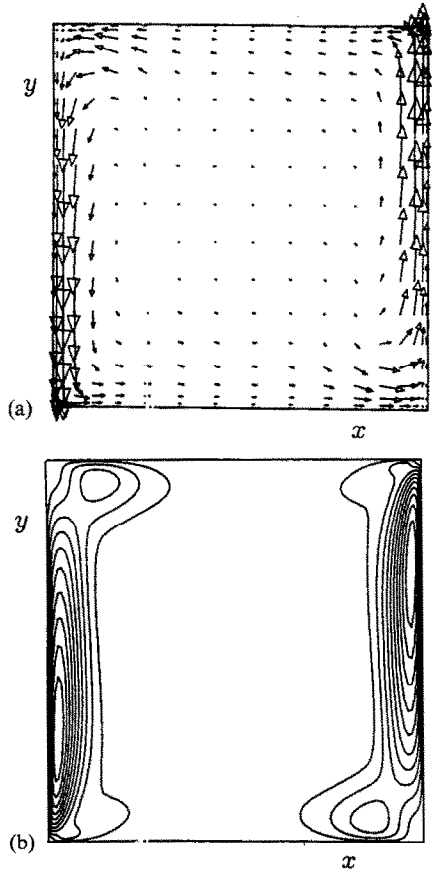


FIG. 3. Shear stress distribution in the plane  $z = 0$  of the cubical cavity at  $Ra = 10^6$  with adiabatic horizontal and lateral walls: (a) shear-stress vectors; (b) shear-stress magnitude.

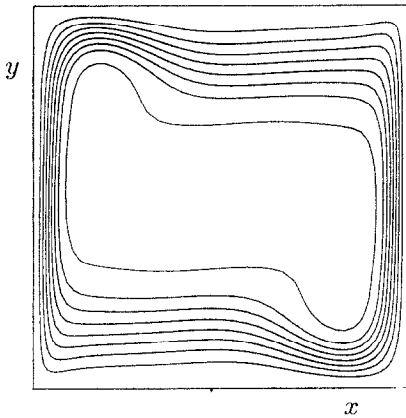


FIG. 4. Streamlines in the two-dimensional square cavity with adiabatic horizontal walls at  $Ra = 10^6$ .

cavity are aligned almost tangentially to the streamlines.

Our results thus indicate that firstly, the flow in the plane  $z = H/2$  of the cubical cavity and the flow in the square cavity are similar and secondly, that a maximum of the velocity occurs near the lateral walls, as predicted analytically for a cylindrical forced-convection flow. This suggests that the flow near the lateral walls is essentially driven by the flow that arises (because of buoyancy) near the vertical midplane ( $z = H/2$ ) of the cavity. This also suggests that the distance in the  $z$ -direction should scale with  $H Ra^{-1/4}$  in the boundary layer. To check this scaling, the profiles of  $v_{max}$  have been plotted for different Rayleigh numbers in Fig. 5. Here,  $v_{max}$  has been scaled with  $(g\beta\Delta TH)^{1/2}$  which is the correct scaling for the vertical velocity near the walls. As can be seen in this figure, the different curves collapse into a single curve up to the maximum and the curves for higher Rayleigh numbers are close together at least up to  $z Ra^{1/4}/H = 10$ , confirming the scaling of the  $z$ -coordinate in the boundary layer along the wall  $z = 0$ .

## 5. UNSTEADY FLOW RESULTS

Beyond a critical Rayleigh number the solution for large time is no longer steady. To investigate the bifurcation to an unsteady flow for air in the cubical, differentially heated cavity, calculations were performed for Rayleigh numbers in the range from  $10^6$  to  $3 \times 10^6$ . The horizontal walls ( $y = 0, H$ ) were considered to be perfectly conducting (i.e.  $T(x) = T_h - (x/H)(T_h - T_c)$ ). The vertical front and back walls ( $z = 0, H$ ) were taken adiabatic.

Both the boundary conditions and the equations again permit the solutions to obey the symmetry relations, given by equations (19) and (20). It has been argued by Henry and Buffat [25] that, in the case of a Hopf-bifurcation (as does occur in the 2D square cavity and probably also in the 3D cubical cavity) either both of these symmetries should be maintained or both of them should be broken. For a differentially heated rectangular cavity (with a height/width ratio of 0.25 and a height/depth ratio of 0.5) with adiabatic horizontal and lateral walls, filled with a low-Prandtl number fluid ( $Pr = 0$  and  $Pr = 0.026$ ), Henry and Buffat [25] found that both symmetries were indeed broken. To check whether these symmetries are also broken for air ( $Pr = 0.71$ ) in the cubical cavity, we performed calculations on a  $30^3$  grid without imposing the symmetries, for a Rayleigh number above the critical value. It was found that in the resulting solution both spatial symmetries were present. Also, the amplitudes and the frequency of the oscillation were the same as those obtained in a calculation on the same grid but with both spatial symmetries imposed. Hence, in all subsequent calculations that were performed, the spatial symmetries were imposed on the solution.

To check the accuracy of our results, calculations have been performed using grids with up to  $120^3$  volumes, for a Rayleigh number of  $2.5 \times 10^6$  which is slightly larger than the critical value at which

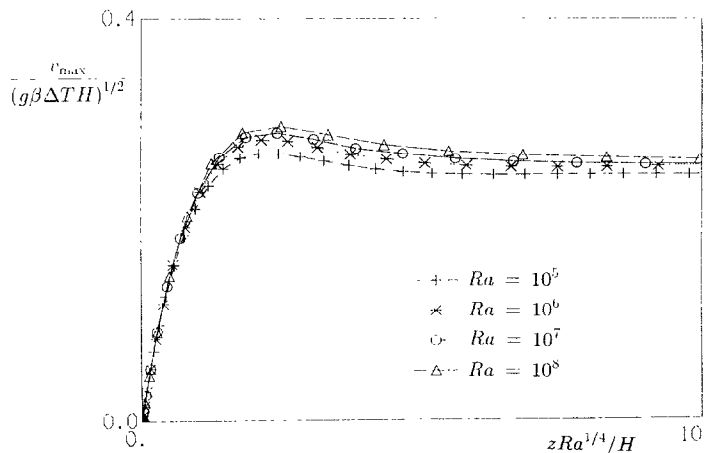


FIG. 5. Scaling of the normal coordinate in the boundary layers along the lateral walls of the cubical cavity, filled with air. The horizontal as well as the lateral walls are adiabatic.

Table 2. Frequency and amplitudes ( $\delta$ ) of the oscillation in characteristic quantities, obtained on the different grids for air at  $Ra = 2.5 \times 10^6$  in the cavity with conducting horizontal and adiabatic lateral walls

| Grid    | $fH/(g\beta\Delta TH)^{1/2}$ | $\delta(\overline{Nu} Ra^{-1/4})$ | $\delta(v_{\max}/(g\beta\Delta TH)^{1/2})$ | $\delta(u_{\max}/(g\beta\Delta T\nu)^{1/3})$ |
|---------|------------------------------|-----------------------------------|--|--|
| $16^3$  | 0.158                        | 0.00724                           | 0.0901                                     | 0.542  |
| $30^3$  | 0.296                        | 0.00255                           | 0.120                                      | 0.118  |
| $60^3$  | 0.263                        | 0.0109                            | 0.115                                      | 0.119  |
| $120^3$ | 0.266                        | $(9.83 \pm 0.24) \times 10^{-3}$  | $0.122 \pm 0.005$                          | $0.139 \pm 0.003$                            |

the flow bifurcates from steady to periodic. On all grids a periodic solution was obtained. It was checked by time-step refinement that a time-step of  $\Delta t\sqrt{(g\beta\Delta TH)}/H = 1/16$  gave almost time-step independent results. The results of these calculations are given in Table 2. Tabulated is the frequency with which the large-time solution oscillates, together with the amplitudes of the oscillations in  $v_{\max}$ ,  $\overline{Nu} Ra^{-1/4}$  and  $u_{\max}$ . For the solution on the  $120^3$  grid the calculation could, because of the limited amount of CPU-time available, not be brought to a full completion (the calculation on the  $120^3$  grid used some 100 h of CPU-time on a single processor of a CRAY-YMP4 and was still not fully converged; contrary to this, a typical calculation on a  $60^3$  grid only took some 9 h of CPU-time to be fully converged). The consequences of this can be seen in Fig. 6, in which the final part of the calculated time-evolution of  $u_{\max}$  on the  $120^3$  grid has been depicted. A small decaying oscillation in the amplitude is still present in the solution after an integration time of  $500H/\sqrt{(g\beta\Delta TH)}$ . This results in small uncertainties in the determination of the amplitudes which have been included in Table 2. For the other grids, the calculations could be continued far enough to damp this oscillation in the amplitudes completely. Unlike the amplitudes, the frequency showed no variation during the evolution of the solution. When the obtained values are compared for the different grids, it can be seen that the differences between the  $60^3$  and  $120^3$  grids are small for the frequency  $f$  and for  $v_{\max}$

(respectively 1.1% and 5.7%), but they are somewhat larger for  $\overline{Nu}$  and  $u_{\max}$  (respectively 11% and 14%). Clearly, the  $16^3$  and the  $30^3$  grids are too coarse to capture all the physics of the flow accurately. At least a  $120^3$  grid is necessary to calculate the flow accurately in all characteristic quantities, although a  $60^3$  grid is sufficient to capture the most important physical aspect accurately, namely the frequency of the oscillation and thus the instability mechanism of the flow. To estimate the critical Rayleigh number, calculations have been performed for different Rayleigh numbers, mainly on the  $60^3$  grid. Based on these calculations, the critical Rayleigh number ( $Ra_{cr}$ ) is estimated to be between  $2.25 \times 10^6$  and  $2.35 \times 10^6$ . This value is only slightly larger than the critical Rayleigh number obtained for the two-dimensional cavity, which was found to be approximately  $2.10 \times 10^6$  (Henkes [3] and Winters [6]). The fact that the critical Rayleigh number for the cubical cavity is slightly larger than for the square cavity seems to be attributable to the larger friction in the 3D-geometry because of the presence of the lateral walls.

Fusegi *et al.* [11] performed a single calculation using a grid with  $62^3$  volumes at  $Ra = 8.5 \times 10^6$ . They found a frequency  $fH/\sqrt{(g\beta\Delta TH)} = 0.33$ , which is 24% larger than the value we have obtained. The most likely reason for this large difference is that Fusegi *et al.* obtained a solution corresponding to a different branch of solutions and the difference is probably unrelated to the large discrepancy in the Ray-

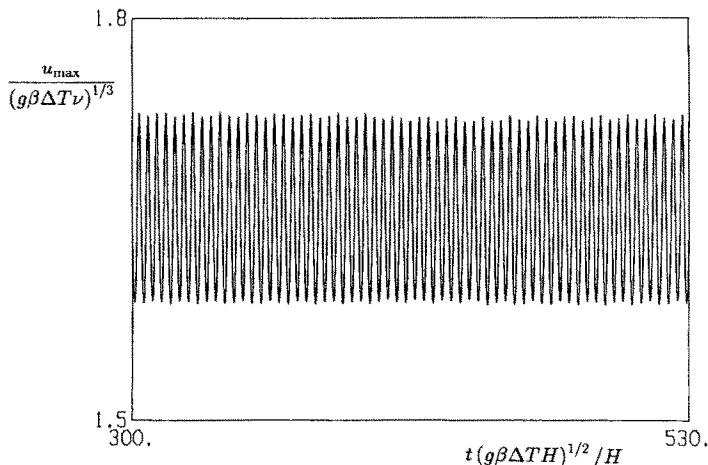


FIG. 6.  $u_{\max}$  as a function of time on the  $120^3$ -grid at  $Ra = 2.5 \times 10^6$  with conducting horizontal walls. Visible are the small variations in the amplitude.

leigh numbers considered (for the 2D square cavity, Henkes [3] found that the frequency, scaled with  $\sqrt{(g\beta\Delta TH)}/H$ , is almost independent of the Rayleigh number). Indeed, for the 2D square cavity, Le Quéré and Alziary de Roquefort [5] obtained three different frequencies,  $fH/\sqrt{(g\beta\Delta TH)} = 0.255, 0.29$  and  $0.32$ , respectively, each corresponding to a different branch. It appears that the highest of these frequencies corresponds to the branch for which Fusegi *et al.* calculated the 3D analogue.

Comparison of the frequency of the oscillation at  $Ra = 2.5 \times 10^6$  in the three-dimensional cubical cavity ( $fH/\sqrt{(g\beta\Delta TH)} = 0.266$ ) with the frequency in the two-dimensional square cavity ( $fH/\sqrt{(g\beta\Delta TH)} = 0.256$ ) and of the (estimated) critical Rayleigh numbers for these cases, shows that the values are indeed close (differences of 4% in the frequency and 10% in the critical Rayleigh number). This suggests that the instability in the three-dimensional cubical cavity is essentially a two-dimensional instability, very similar to the one observed in the two-dimensional cavity. To investigate this point more closely, the time dependence of the temperature perturbation for  $Ra = 2.5 \times 10^6$  has been visualized. To obtain the perturbation, in every grid point the local time-averaged temperature has been subtracted from the local instantaneous temperature at several instants during one period of the oscillation. This results in the appearance of hot and cold spots at those places where the local instantaneous temperature at the depicted time-instant is higher/lower than the local time-averaged temperature. The growth, movement and decay of these spots can be seen in Fig. 7, which shows eight equidistant time-instants of one single period of the oscillation in the plane  $z = H/2$ . The birth of a hot spot in the lower left corner can be seen clearly (at the arrow). This spot travels up along the left vertical wall until it is dissipated in the upper part of the vertical boundary layer after about 3/2 periods. Because of the symmetry of the flow, a similar pattern can be found in the right half of the plane. The same evolution of hot and cold spots was found in the case of the two-dimensional square cavity by Henkes [3] again suggesting that the instability mechanisms in the two- and three-dimensional geometries are the same.

These results suggest that the no-slip boundary conditions at the lateral walls do not change the instability mechanism fundamentally. To investigate the influence on the instability mechanism of the thermal boundary condition at the lateral walls, these walls were taken perfectly conducting instead of adiabatic (i.e. a linear temperature profile was prescribed on these walls). The frequency of the oscillation on the  $60^3$  grid at  $Ra = 2.5 \times 10^6$  was found to be  $fH/\sqrt{(g\beta\Delta TH)} = 0.276$ , only 3.8% larger than in the case of adiabatic lateral walls. This suggests that the instability mechanism responsible for the first bifurcation, is not very susceptible to the thermal boundary conditions applied at the lateral walls and again con-

firms the idea that the first instability is mainly of a two-dimensional nature.

The probable origin of the instability and the resulting oscillation in the flow can be understood from Fig. 8. It shows the isotherms in the plane  $z = H/2$  at a Rayleigh number of  $2.0 \times 10^6$  which is only slightly below the critical value. The important feature in the flow can be found in the horizontal boundary layers and especially in the lower left and upper right corners (which were also the places where the hot and cold spots originated from). In these regions, the vertical temperature gradient  $\partial T/\partial y$  is negative, i.e. the temperature decreases and hence the density increases with height. In these regions therefore, light fluid is below heavy fluid and it is a well-established fact from hydrodynamic stability theory (see, e.g. Drazin and Reid [26]) that the occurrence of such a density distribution in a flow can lead to an instability and oscillations. The notion that this unstable density gradient is responsible for the oscillation is supported by Fig. 9, which shows the amplitude of the oscillation in the temperature in the plane  $z = H/2$ . Clearly, the magnitude of the oscillations is largest in the lower left and upper right corners.

Although these results indicate that the mechanism behind the first instability in the 3D cubical cavity is of a two-dimensional nature, it must be expected that the oscillations in the cavity are also influenced by the presence of the lateral walls. That there is indeed a marked influence of these walls on the structure of the oscillations, is shown in Figs. 10(a) and (b). In Fig. 10(a), the contour lines of equal amplitude of the temperature oscillations in the plane  $y = H/10$  for  $Ra = 2.5 \times 10^6$  are shown. The amplitude has a somewhat surprising and distinct distribution as a function of depth ( $z$ ). That there is indeed a regular pattern, is shown in Fig. 10(b), which shows the amplitude as a function of  $z$  at  $x = 0.048H$  in the plane  $y = H/10$ . Figure 11(b) suggests, that the influence of the lateral walls leads to a regular, wave like pattern in the  $z$ -direction. For the cubical cavity, the wavelength is approximately 1/3 the cavity depth. To check this influence of the lateral walls on the structure of the oscillating flow further, calculations were performed for two cavities with different depth/height ( $A_z$ ) aspect ratios, namely for  $A_z = 2$  and for  $A_z = 0.5$ . In both cases, the flow just after the first bifurcation was calculated: for the cavity  $A_z = 2$ , the Rayleigh number taken was  $2.5 \times 10^6$  and for the cavity with  $A_z = 0.5$  it was  $6 \times 10^6$ . The amplitude distributions in the plane  $y = H/10$  and along the line  $x = 0.048H$  in the plane  $y = H/10$  are shown in Figs. 11(a), (b) ( $A_z = 2$ ) and 12(a), (b) ( $A_z = 0.5$ ). As is evident from these figures, the wave like pattern is present for  $A_z = 2$  (with a wavelength of approximately 1/5 the cavity depth). For the cavity with  $A_z = 0.5$ , there is no wave-like pattern. The amplitude is roughly constant over approximately 70% of the cavity depth and then drops off. Basically, this looks very much like an extension of the 2D-amplitude distribution, stretched in the  $z$ -

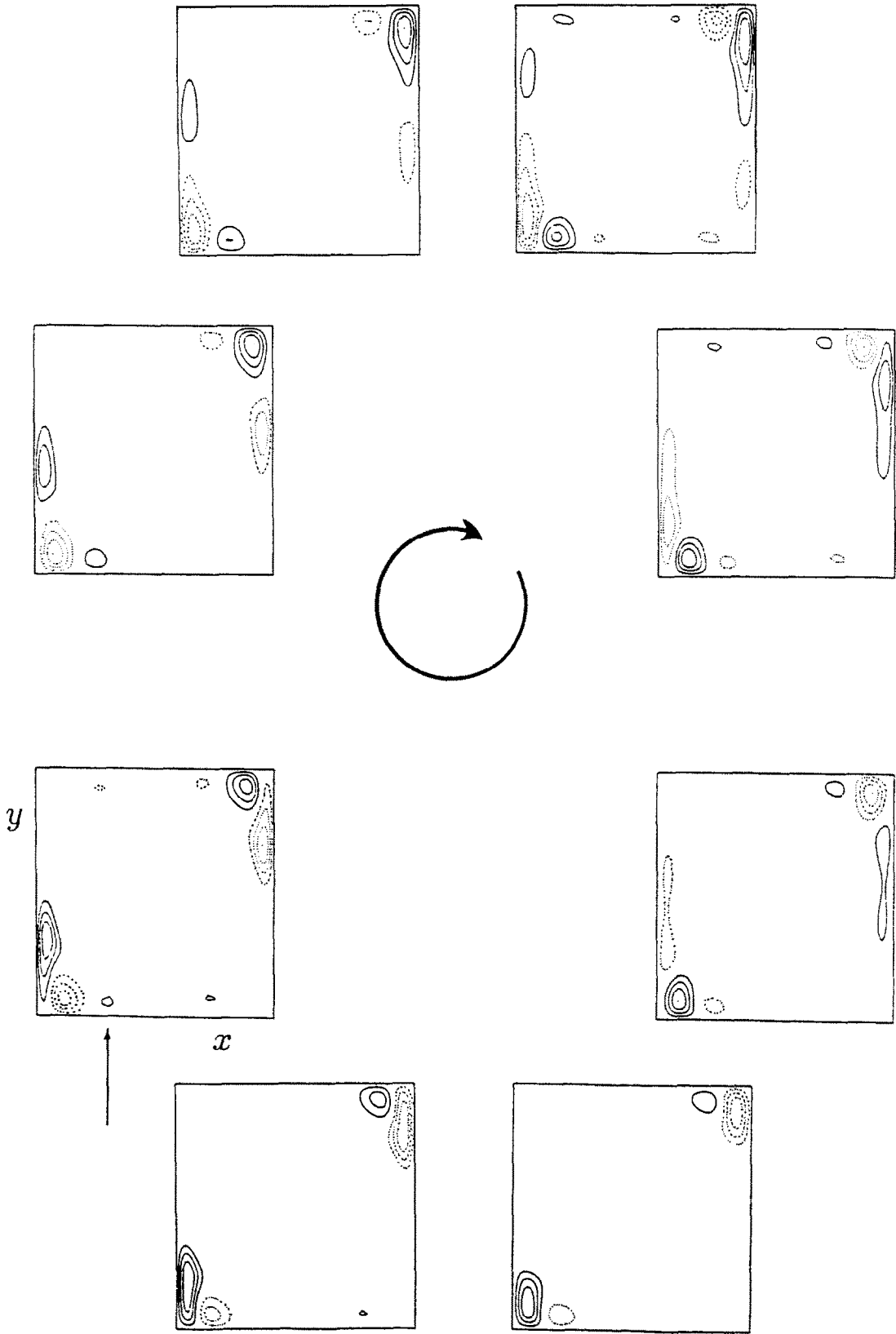


FIG. 7. Temperature perturbations, during one period of the oscillation, in the vertical midplane  $z = H/2$  of the cubical cavity at  $Ra = 2.5 \times 10^6$  with conducting horizontal walls. The birth of a hot spot occurs at the arrow. Dotted contour lines correspond to cold spots.

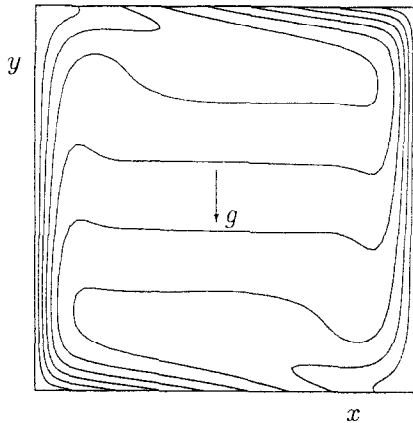


FIG. 8. Isotherms in the vertical midplane  $z = H/2$  of the cubical cavity at  $Ra = 2 \times 10^6$  with conducting horizontal walls. Note the unstable temperature distribution near the lower left and upper right corners of the plane.

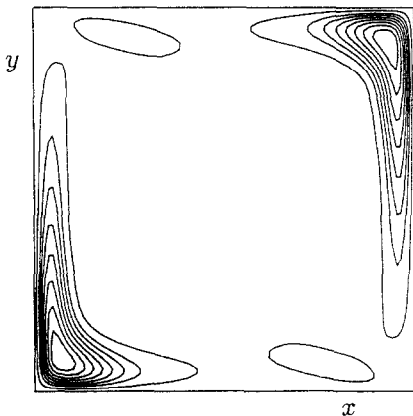


FIG. 9. Amplitude of the temperature oscillations in the vertical midplane  $z = H/2$  of the cubical cavity at  $Ra = 2.5 \times 10^6$  with conducting horizontal walls.

direction and modified only in the boundary layers along the lateral walls. Hence, if the cavity depth is equal to or larger than its width, the lateral walls change the structure of the oscillating flow in the third dimension over the entire depth of the cavity, whereas the structure is changed only in the boundary layers along the lateral walls if the cavity depth is equal to half the cavity width.

It is interesting to note that Penot *et al.* [27] performed a stability analysis of the 2D-flow for instabilities in the third dimension. They studied the stability of the flow in a cavity with a height/width-ratio of 4 and with adiabatic horizontal walls. The stability analysis was performed by taking the solution of the Navier-Stokes equations for the 2D cavity and extending it in the third dimension through an expansion in a Fourier-series and by applying *periodic* boundary conditions in this third dimension. Penot *et al.* noted that for a 3D-cavity with its depth equal to its width, the 2D-solution was unstable to a 3D-

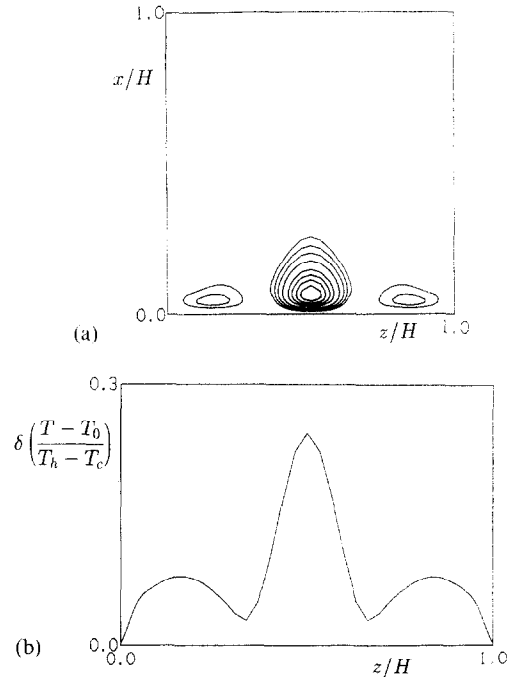


FIG. 10. Three-dimensionality in the distribution of the amplitude of temperature oscillations in the cubical cavity with conducting horizontal walls at  $Ra = 2.5 \times 10^6$ . (a) Contour lines in the plane  $y = H/10$ ; (b) amplitude distribution in the plane  $y = H/10$  along the line  $x = 0.048H$ .

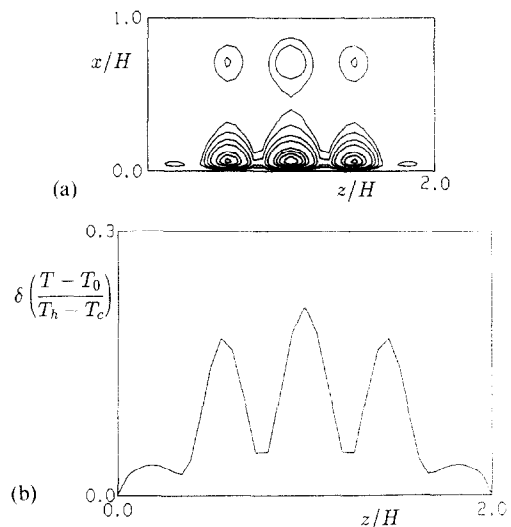


FIG. 11. Same as for Fig. 10 but for the cavity with  $Ar = 2$ .

instability. This instability only had a small influence on the mean flow and did *not* introduce new frequencies in the flow. Also, for a cavity with its depth equal to half its width, no such instability appeared. Although this stability analysis was performed for a configuration different from the one for which our direct simulations were performed, there seems to be close agreement between the obtained results. The structure of the oscillating flow is mainly two-dimensional for a cavity with its depth equal to half its width and becomes three-dimensional if the depth becomes

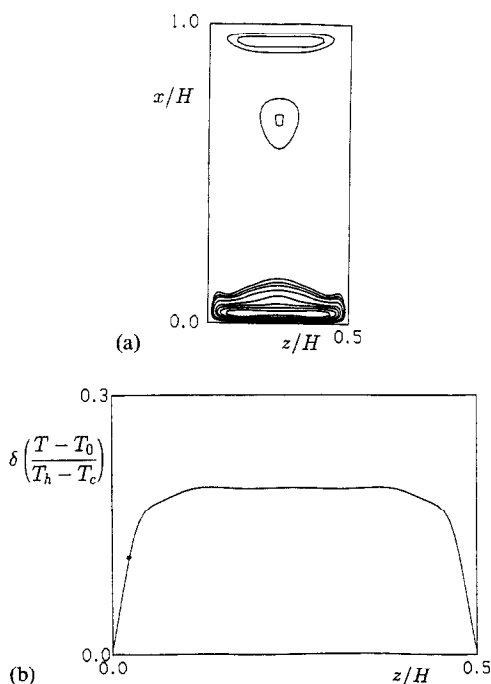


FIG. 12. Same as for Fig. 10 but for the cavity with  $A_z = 0.5$  at  $Ra = 6 \times 10^6$ .

larger than or equal to the cavity width. The mean flow, however, is not changed significantly (except near the lateral walls) and is mainly two-dimensional.

Apart from the remarkable structure in the  $z$ -dependence of the amplitude of the temperature oscillation, the three-dimensionality also leads to clearly detectable phase differences between oscillations at different  $z$ -positions inside the cavity. For the cubical cavity, these phase differences have been depicted in Fig. 13. This figure shows, for the line  $(x/H, y/H) = (0.048, 0.1)$ , both the  $z$ -dependence of the amplitude in the temperature oscillation as well as the phase differences between the temperature oscillations at the marked

positions compared with the temperature oscillation at the vertical midplane  $z = H/2$ . Here, the phase difference is taken to be negative (i.e. it is assumed that the oscillation at  $z = H/2$  leads the oscillations at all other locations). Clearly, the phase differences are correlated with the distribution of the amplitude: the phase differences are small within a peak in the amplitude distribution. Near the minimum values ('nodes') of the amplitude, however, there is a large jump in the phases. This behaviour is, in principle, similar to the behaviour of a standing-wave like oscillation. However, for a true standing-wave, the jumps in the phases would be  $\pi$  in magnitude, whereas the jumps in the present situation are only approximately  $\pi/2$  in magnitude.

## 6. CONCLUSIONS

Both the steady and the periodic flow regime have been investigated in an air-filled differentially heated cubical cavity.

For the steady flow regime, the top/bottom and front/back walls of the cavity were taken adiabatic. For  $Ra = 10^6$ , systematic grid refinement up to  $120^3$  grid points, showed that accurate results were obtained. It was found that the calculated results for the cubical cavity differed only little from those obtained for the square cavity and that the influence of the front/back (lateral) walls is restricted mainly to a small portion of the cavity, adjacent to these walls, where a boundary layer is formed. By performing calculations for several different Rayleigh numbers, it was checked that the coordinate perpendicular to the lateral walls scales with  $H Ra^{-1/4}$ .

The periodic flow regime has been studied mainly for the situation that the top/bottom walls were taken perfectly conducting, whereas the front/back walls were adiabatic. The flow becomes unsteady at a critical Rayleigh number which is estimated to be between

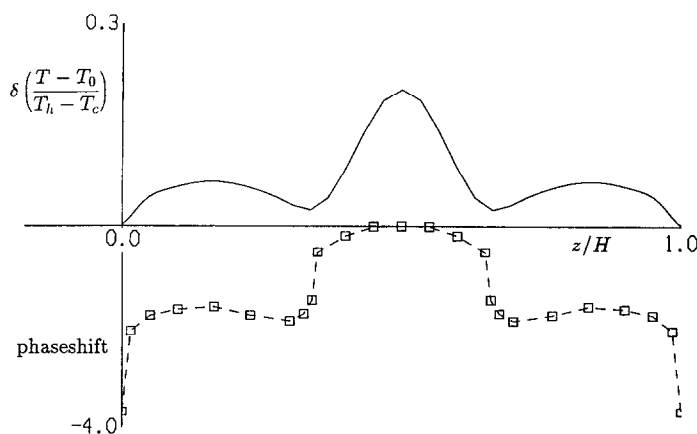


FIG. 13. Three-dimensionality in the temperature oscillations in the cubical cavity with conducting horizontal walls at  $Ra = 2.5 \times 10^6$ . The  $z$ -dependence of the amplitude in the temperature oscillations (upper half of the plot) as well as the phase differences relative to  $z = H/2$  (lower half of the plot) have been depicted in the plane  $y = H/10$  along the line  $x = 0.048H$ .

$2.25 \times 10^6$  and  $2.35 \times 10^6$ , some 10% larger than in the square cavity. The amplitudes in the oscillations showed some grid-dependence even though grids with up to  $120^3$  grid points were employed. The frequency however, was grid-independent and found to be  $fH/\sqrt{(g\beta\Delta TH)} = 0.266$ , only 4% larger than the value found in the square cavity at the same Rayleigh number. Also the time-evolution of temperature perturbations in the plane  $z = H/2$  of the cubical cavity was similar to the evolution observed in the square cavity. This suggests that the same type of instability occurs both in the two-dimensional and the three-dimensional cavity. The isotherms in the steady flow just below the critical Rayleigh number show that in the horizontal boundary layers, density increases with height. It is well known that this is an unstable distribution which is related to the Rayleigh-Bénard instability. That this unstable density distribution is indeed responsible for the bifurcation is suggested by the time-evolution of the temperature perturbations, which are created in this unstable region and by the amplitudes of the oscillations which are largest in this region.

The influence of the lateral walls in the cubical cavity is most pronounced if the structure of the oscillating flow is considered. The amplitude of the temperature oscillations has a regular, wave like pattern as a function of the depth. This pattern is also found if the depth is increased to twice the cavity width but it disappears if the depth is reduced to half the cavity width. The amplitude is then modified only in thin layers near the lateral walls. Although obtained for a configuration somewhat different from ours, the results of a stability analysis, performed by Penot *et al.* [27], of the 2D flow seem to be in agreement with our results.

*Acknowledgements*—The authors wish to thank the ‘Stichting voor Fundamenteel Onderzoek der Materie’ (FOM) and the Royal Netherlands Academy of Arts and Sciences (KNAW) for providing support through research grants. Thanks are also due to the ‘Stichting Nationale Computer Faciliteiten’ (NCF) which made it possible through grant SC-199 to use the CRAY-YMP computer.

## REFERENCES

- G. de Vahl Davis and I. P. Jones, Natural convection in a square cavity: a comparison exercise, *Int. J. Numer. Meth. Fluids* **3**, 227–248 (1983).
- R. J. A. Janssen and R. A. W. M. Henkes, Accuracy of the finite-volume discretization for the bifurcating natural-convection flow in a heated square cavity, *Numer. Heat Transfer* (in press).
- R. A. W. M. Henkes, Natural-convection boundary layers, Ph.D. Thesis, Delft (1990).
- P. Le Quéré and T. Alziary de Roquefort, Transition to unsteady natural convection of air in differentially heated cavities: influence of thermal boundary conditions on the horizontal walls, *Proc. 8th Int. Heat Transfer Conf.*, pp. 1533–1538, Hemisphere, San Francisco (1986).
- P. Le Quéré and T. Alziary de Roquefort, On the existence of multiple periodic solutions of the Boussinesq equations, *Mech. Fluids*, C.R. Acad. Sci. Paris, Vol. 306 II, 681–687 (1988).
- K. H. Winters, Hopf bifurcation in the double-glazing problem with conducting boundaries, *J. Heat Transfer* **109**, 894–898 (1987).
- D. N. Jones and D. G. Briggs, Periodic two-dimensional cavity flow: effect of linear horizontal thermal boundary condition, *J. Heat Transfer* **111**, 86–91 (1989).
- G. D. Mallinson and G. de Vahl Davis, Three-dimensional natural convection in a box: a numerical study, *J. Fluid Mech.* **83**, 1–31 (1977).
- Y. Le Peutrec and G. Lauriat, Effects of the heat transfer at the side walls on natural convection in cavities, *J. Heat Transfer* **112**, 370–378 (1990).
- T. Fusegi, J. M. Hyun, K. Kuwahara and B. Farouk, A numerical study of three-dimensional natural convection in a differentially heated cubical enclosure, *Int. J. Heat Mass Transfer* **34**, 1543–1557 (1991).
- T. Fusegi, J. M. Hyun and K. Kuwahara, Three-dimensional numerical simulation of periodic natural convection in a differentially heated cubical enclosure, *Appl. Sci. Res.* **49**(3), 271–282 (1992).
- S. V. Patankar and D. B. Spalding, A calculation procedure for heat, mass and momentum transfer in three-dimensional parabolic flows, *Int. J. Heat Mass Transfer* **15**, 1787–1806 (1972).
- F. H. Harlow and J. E. Welch, Numerical calculation of time-dependent viscous incompressible flow of fluid with free surface, *Physics Fluids* **8**, 2182–2189 (1965).
- J. Van Kan, A second-order accurate pressure-correction scheme for viscous incompressible flow, *SIAM J. Sci. Stat. Comput.* **7**, 870–891 (1986).
- J. A. Meijerink and H. A. Van der Vorst, An iterative solution method for linear systems of which the coefficient matrix is a symmetric M-matrix, *Maths Comput.* **31**, 148–162 (1977).
- H. A. Van der Vorst, High performance preconditioning, *SIAM J. Sci. Stat. Comput.* **10**, 1174–1185 (1989).
- P. F. Dubois, A. Greenbaum and G. H. Rodrigue, Approximating the inverse of a matrix for use in iterative algorithms on vector processors, *Computing* **22**, 257–268 (1979).
- H. A. Van der Vorst, A vectorizable variant of some ICCG methods, *SIAM J. Sci. Stat. Comput.* **3**, 350–356 (1982).
- J. J. F. M. Schlichting and H. A. Van der Vorst, Solving 3D block bidiagonal linear systems on vector computers, *J. Comp. Appl. Math.* **27**, 323–330 (1989).
- P. Haldenwang and G. Labrosse, 2-D and 3-D spectral Chebyshev solutions for free convection at high Rayleigh number, *Proc. 6th Int. Symposium on Finite Element Methods in Flow Problems*, pp. 261–266 (1986).
- P. Le Quéré, Accurate solutions to the square thermally driven cavity at high Rayleigh number, *Comput. Fluids* **20**, 29–41 (1991).
- U. T. Bödewadt, Die Drehströmung über festem Grunde, *Z. Angew. Math. Mech.* **20**, 241–253 (1940).
- A. E. Gill, The boundary-layer regime for convection in a rectangular cavity, *J. Fluid Mech.* **26**, 515–536 (1966).
- W. P. Graebel, The influence of Prandtl number on free convection in a rectangular cavity, *Int. J. Heat Mass Transfer* **24**, 125–131 (1981).
- D. Henry and M. Buffat, Two and three-dimensional numerical simulations of the transition to oscillatory convection in low-Prandtl number fluids, Report Lab. de Méc. des Fluides et d’Acoust. (ECL) (1991).
- P. G. Drazin and W. H. Reid, *Hydrodynamic Stability*, Cambridge University Press, Cambridge, U.K. (1981).
- F. Penot, A. N’Dame and P. Le Quéré, Investigation of the route to turbulence in a differentially heated cavity, *Proc. 9th Int. Heat Transf. Conf.*, Vol. 2, pp. 417–422, Jerusalem (1990).